An integrated bulk and surface modification strategy for gas-quenched inverted perovskite solar cells with efficiencies exceeding 22%

Xin Zhang, Weiming Qiu*, Wenya Song, Zafer Hawash, Yaxin Wang, Bapi Pradhan, Yiyue Zhang, Denys Naumenko, Heinz Amenitsch, Ellen Moons, Tamara Merckx, Aranzazu Aguirre, Yaser Abdulraheem, Tom Aernouts, Yiqiang Zhan*, Yinghuan Kuang*, Johan Hofkens, Jef Poortmans*

X. Zhang, Y. Wang, Y. Zhan
Center for Micro Nano Systems
School of Information Science and Technology (SIST)
Fudan University
Handan 220, Shanghai 200433, China
E-mail: yqzhan@fudan.edu.cn

X. Zhang, W. Song, J. Poortmans
Department of Electrical Engineering (ESAT)
KU Leuven
Kasteelpark Arenberg 10, 3001 Leuven, Belgium

X. Zhang
Academy for Engineering & Technology (FAET)
Fudan University
Handan 220, 200433 Shanghai, China

X. Zhang, W. Song, T. Merckx, A. Aguirre, T. Aernouts, Y. Kuang, J. Poortmans
Imec, imo-imomec, Thin Film PV Technology – partner in Solliance
Thor Park 8320, Genk 3600, Belgium
E-mail: Yinghuan.Kuang@imec.be, Jef.Poortmans@imec.be

X. Zhang, W. Song, T. Merckx, A. Aguirre, T. Aernouts, Y. Kuang, J. Poortmans
imo-imomec
EnergyVille
Thor Park 8320, 3600 Genk, Belgium

X. Zhang, W. Song, T. Merckx, A. Aguirre, T. Aernouts, Y. Kuang, J. Poortmans
imo-imomec
Hasselt University
Martelarenlaan 42, 3500 Hasselt, Belgium

W. Qiu
imec - SAT department
Kapeldreef 75, Leuven 3001, Belgium
E-mail: Weiming.Qiu@imec.be

W. Qiu, B. Pradhan, Y. Zhang, J. Hofkens
Department of Chemistry
KU Leuven
Celestijnenlaan 200F, Leuven 3001, Belgium

Z. Hawash, E. Moons

Department of Engineering and Physics
Karlstad University
Karlstad SE-651 88, Sweden

D. Naumenko, H. Amenitsch
Institute of Inorganic Chemistry
Graz University of Technology
Stremayrgasse 9/V, Graz 8010, Austria

Y. Abdulraheem
Department of Electrical Engineering
Kuwait University
P.O. Box 5969, Safat 13060, Kuwait

Keywords: gas quenching, benzylammonium thiocyanate, surface treatment, additive engineering, inverted p-i-n perovskite solar cells, stability

Inverted perovskite solar cells (PSCs) prepared by anti-solvent method have achieved power conversion efficiencies (PCEs) of over 23%, but they are not ideal for device upscaling. Conversely, gas-quenched PSCs offer great potential for upscaling, but their performance still lags behind. Herein, we seek to upgrade the gas-quenched films through both surface and bulk modifications. First, a novel surface modifier, benzylammonium thiocyanate (BASCN), is found to allow remarkably improved surface properties, but the PCE gain is limited by the existence of longitudinally multiple grains. Thus, we further utilize methylammonium chloride (MACl) additive as a second modifier to realize monolithic grains. Such an integrated strategy enables the average open-circuit voltage (V_{oc}) of the gas-quenched PSCs to increase from 1.08 V to 1.15 V, leading to a champion PCE of 22.3%. Moreover, the unencapsulated device shows negligible degradation after 150 h of maximum power point operation under simulated 1 sun illumination in N_2.

1. Introduction

Organic-inorganic hybrid perovskite solar cells (PSCs) have been recognized as a potential game-changer in the photovoltaic (PV) field. In the past years, both the power conversion efficiency (PCE) and the long-term operational stability of PSCs have been significantly improved through composition modulation,[1–3] bulk and interfacial defect passivation,[4–6] and device architecture optimization.[7–9] In particular, multifunctional molecules are of increasing interest as they can effectively passivate various defects and construct more stable perovskites surface by forming stronger Pb-S, Pb-O and other interactions.[10–13] Remarkably, PSCs that can successfully pass the stability criteria test of IEC61215:2016 standards have been

reported,[14] which is a huge step towards the industrialization and commercialization of this PV technology.

Throughout the development history of PSCs, improving the perovskite film quality has always been the key to achieving highly efficient and stable devices. This insight has driven the development of diverse film deposition techniques, including anti-solvent assisted deposition,[15] sequential deposition,[16] vacuum assisted deposition,[17] the gas quenching technique and so on.[18,19] Among them, anti-solvent assisted deposition is favored since it allows the fabrication of highly efficient devices. Nevertheless, this technique is not compatible with large-area manufacturing. In contrast, the gas quenching method has great potential for cost-effective and large-area device manufacturing, but the performance of gas-quenched devices is currently lower than that of the state-of-the-art devices fabricated with anti-solvent assisted deposition.[20–23] So far, with various film and device optimization strategies, highly efficient gas-quenched n-i-p PSCs with a best PCE of 23.6% have been reported.[24–27] As for the gas-quenched inverted p-i-n PSCs, Liu et al. obtained PCEs of 22.07% by using a multifunctional sulfobetaine-based zwitterionic surfactant to improve the film quality.[28] Recently, Chen et al. reported that partially replacing dimethyl sulfoxide with the solid-state lead-coordinating additive carbohydrazide can reduce the formation of voids at the hole transport layer/perovskite interface, yielding a PCE of 23.8% for inverted PSCs fabricated with a N_2 knife.[29]

Despite those mentioned progress, further insights are still required to understand the factors that limit the performance of the gas-quenching PSCs. In this work, we show that it is important to synergistically upgrade both the surface and bulk properties of the gas-quenched perovskite films to achieve the optimal performance of the corresponding PSCs. Taking an integrated modification strategy, i.e., using benzylammonium thiocyanate (denoted as BASCN) as a modifier for perovskite surface and methylammonium chloride (MACl) as an additive for perovskite bulk formation, we obtain a significant PCE boost for our inverted p-i-n gas-quenched PSCs, with a champion efficiency of 22.3%. Furthermore, the resulting devices also show negligible degradation after 150 h of operation at the maximum power point (MPP) under simulated 1 sun illumination at a temperature of ~60 °C. Thus, this work provides further guidelines for the development of high-efficiency and stable gas-quenched inverted PSCs.

2. Results and Discussion

Although surface passivation using Lewis acids/bases,[30] ionic liquids,[31] and low-dimensional capping layers,[32–35] has been widely applied to perovskite films prepared by the anti-solvent method, ligands containing both ammonium cations and pseudo halide anions are scarcely studied for this purpose, especially on gas-quenched perovskite films. Based on a Cs-FA dual-cation lead halide perovskite, we first prove that BASCN, as a surface modifier, can induce the recrystallization of the perovskite film, resulting in larger grains, longer carrier lifetime, and a suitable band bending for charge carrier extraction, leading to an increase of the average PCE of gas-quenched inverted PSCs from 17.7% to 19.0%. **Figure 1a** illustrates the gas quenching and the BASCN treatment procedures used in this work. After spin coating the perovskite precursor solution, the sample was blown vertically from the top using high pressure nitrogen gas flow (~ 6 Bar) to rapidly extract the solvents, followed by a thermal annealing process to promote the perovskite crystallization. For the perovskite surface treatment, a BASCN solution in IPA was spin-coated on top of the perovskite film after the film has cooled to room temperature, and a post-annealing process was then applied.

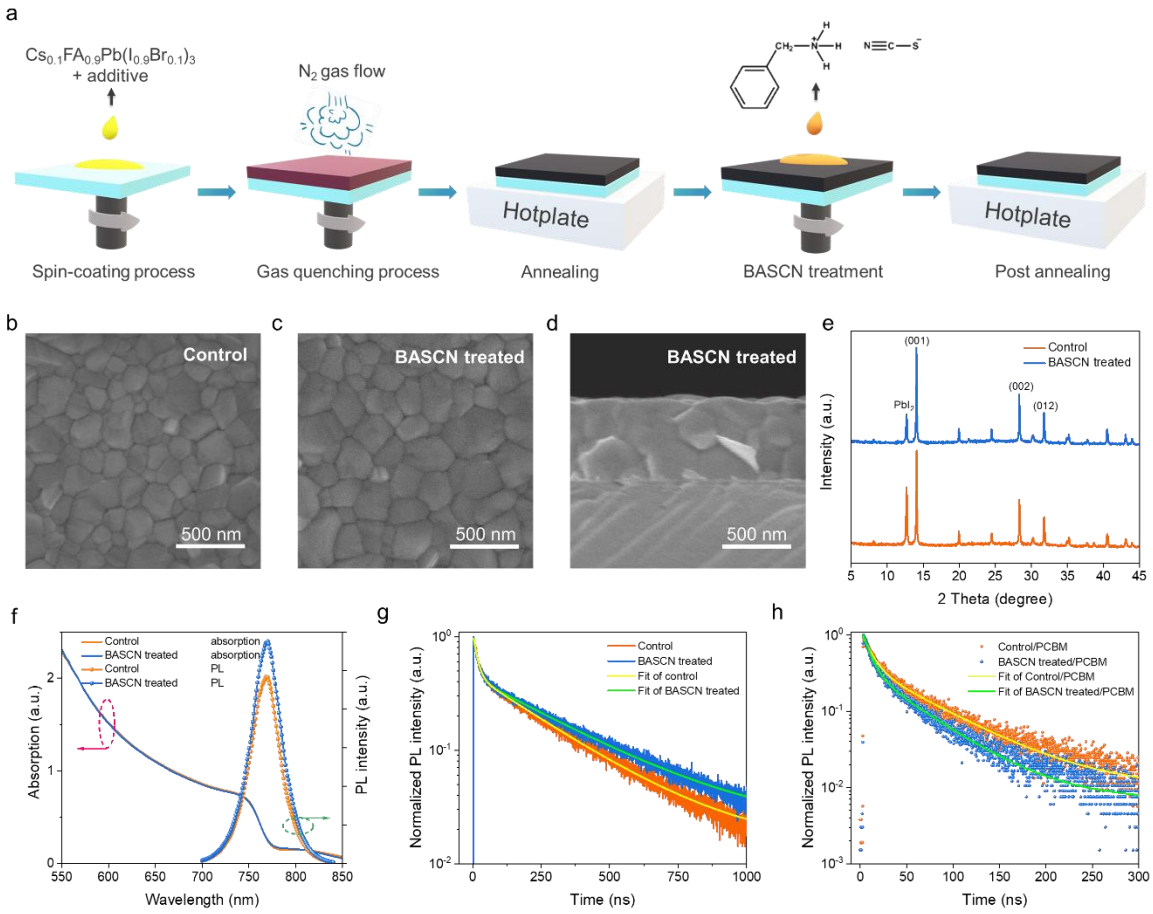

Figure 1. (a) The schematic diagrams illustrate the gas quenching and the BASCN treatment procedures. Top-view SEM images of (b) the control and (c) the BASCN treated perovskite films. (d) Cross-sectional SEM image of the BASCN treated perovskite film. (e) XRD

patterns and (f) UV-Vis absorption spectra and SSPL spectra of the control and the BASCN treated perovskite films. (g) TRPL spectra of the corresponding perovskite films deposited on bare glass. (h) TRPL spectra of PCBM/perovskite films on bare glass, where PCBM acts as a charge quenching layer. The perovskite is $Cs_{0.1}FA_{0.9}Pb(I_{0.9}Br_{0.1})_3$ with 2.75 mol% $PbCl_2$ as additive.

We first explore the effect of BASCN treatment using a dual-cation perovskite $Cs_{0.1}FA_{0.9}Pb(I_{0.9}Br_{0.1})_3$ prepared using 2.75 mol% $PbCl_2$ as additive. **Figure 1b** and **c** display top-view scanning electron microscopy (SEM) images of the control and the BASCN treated perovskite films, respectively. Clearly, an interaction between perovskite and BASCN has taken place as larger grains were obtained after the treatment. The number of perovskite grains with a size smaller than 100 nm has largely decreased, reducing the grain boundaries, which are often associated with defects.[36] Unfortunately, the increase in grain size occurs mainly in the lateral direction. As displayed in **Figure 1d**, the ~500 nm thick layer consists of 2-3 grains stacked on each other in the longitudinal direction, which hinders an efficient charge transport. Therefore, further optimization in this direction was carried out and will be discussed later.

Figure 1e shows the X-ray diffraction (XRD) patterns of the corresponding perovskite films. Both the control and the BASCN treated films show main diffraction peaks at ~14.0°, 28.3° and 31.7°, classifying as the (001), (002), and (012) planes of cubic perovskite.[37] A typical signal attributed to PbI_2 residue is observed in both cases. This is because an extra lead source ($PbCl_2$) was introduced as additive to the perovskite precursor. Ultraviolet-Visible (UV-Vis) absorption spectra and steady-state photoluminescence (SSPL) spectra are shown in **Figure 1f**. Similar absorption spectra and PL peaks centered at ~770 nm are observed for the control and the BASCN treated perovskite films. However, the BASCN treated sample shows higher PL intensity, which can be an indication of defect reduction. A time-resolved photoluminescence (TRPL) study was then carried out on perovskite films deposited on bare glass to provide an assessment of minority carrier lifetime, which has a strong correlation to the number of defects (**Figure 1g**). The experimental data are fitted with a bi-exponential function (**equation S1**) to yield a fast decay lifetime and a slow decay lifetime, representing the surface charge trapping process and the bulk de-trapping or recombination process, respectively.[28] The average carrier lifetime is calculated accordingly (**equation S2**). Detailed parameters are summarized in **Table S1**. The average carrier lifetime increases from the initial 245.9 ns for the control perovskite to 299.6 ns for the BASCN treated perovskite,

indicating that the non-radiative recombination is suppressed upon the BASCN treatment. It has been demonstrated that the reduced trap density has an influence on the carrier characteristics, i.e. carrier mobility and diffusion length.[38] TRPL of perovskite films with PCBM as the quencher was also measured (**Figure 1h, Table S2**). The corresponding average carrier lifetimes are 51.4 ns and 37.9 ns for the control and the BASCN treated films, respectively. Calculations (**equation S3** and **S4**) indicate that the diffusion length (L) is improved from ~931 nm to ~1225 nm, and the electron mobility (μ) is improved from 1.37 $cm^2\,V^{-1}\,s^{-1}$ to 1.94 $cm^2\,V^{-1}\,s^{-1}$ after the BASCN treatment, showing better carrier transport characteristics, which can contribute to the enhanced photovoltaic device performance.

An X-ray photoelectron spectroscopy analysis (XPS) was conducted to further study the effect of the BASCN treatment on the surface chemical composition, focusing on the major elements of the perovskite, including C, N, Pb and I (**Figure S1**). As shown in the C 1s spectra (**Figure S1a**), there are two characteristic peaks for all perovskite conditions, i.e., the one located at the higher binding energy is attributed to the $C{=}NH_2$ in the FA^+ species, while the one located at the lower binding energy includes contributions from C-H, C-C, C-N in the FA^+ and BA^+ species. Upon post-annealing, there is a clear shift of the peak from 285.1 eV to higher binding energies as the amount of BASCN increases, getting close to that observed in pure BASCN at a slightly higher binding energy. It should be noted that the high binding energy shoulder located at about 288 eV in the pure BASCN spectrum can be attributed to the C-S bond. As shown in **Figure S1b**, we also observed a ~0.1 eV shift of the N 1s peak to lower binding energy when modifying the surface with a high concentration of BASCN. The broad peak at about 400 eV in the N 1s spectrum of pure BASCN can be attributed to the $C\text{-}NH_3^+$ and SCN^- species. Notably, as shown in **Figure 2a**, when compared to the control perovskite, the atomic percentages of both C and N elements on the perovskite surface increase with increasing the BASCN concentration, which proves that BA^+ cations are present on the surface. The existence of BA^+ can be further supported by the decreasing N/C ratio. **Figure S1d** and **e** show the XPS spectra of Pb $4f_{7/2}$ (located at ~138.6 eV), and I $3d_{5/2}$ (located at ~ 619.5 eV), respectively. After introducing BASCN on the surface but without applying post-annealing, the Pb 4f peak is shifted to higher binding energy, implying that the chemical environment of the Pb atom has changed. As revealed by a previous study,[39] SCN^- ions that remained at the surface have strong affinity to Pb^{2+}, and they can even displace the I^- to coordinate with Pb^{2+}. The formed strong Pb-SCN interaction causes the Pb 4f peak to shift towards a higher binding energy.[40] However, when a short post-annealing process is applied, the Pb 4f peak is shifted back to lower binding energies. This shift is more significant with a

higher concentration of BASCN introduced atop the perovskite (labelled as ++ BASCN + anneal). It has been reported recently that isopropyl alcohol (IPA) triggers the reconstruction of the perovskite surface towards a PbI_2-rich upper surface, forming FA^+ vacancies and promoting the adsorption of organic ammonium salts on the perovskite surface.[41] This means that IPA, which is used as the solvent in BASCN solution in this case, can solubilize some of the FA^+ ions on the surface. The introduced SCN^- ions may form volatiles with these FA^+ ions under heat and subsequently dissociate from the surface. The BA^+ ions could therefore enter and passivate these FA^+ vacancy defects. The possible reaction process at the surface is shown in formula (1):

$$FA_xCs_{1-x}PbI_yBr_{3-y} + BA^+ + SCN^- \rightarrow BA_zFA_{x-z}Cs_{1-x}PbI_yBr_{3-y} + FASCN\uparrow \quad (1)$$

Through this reconstruction process, the introduced BA^+ cations at the perovskite surface can form hydrogen bonding interactions with the adjacent I in the PbI_6^{4-} octahedra due to the presence of ammonium heads, which increases the bond length and reduces the bond strength of Pb-I, causing Pb 4f and I 3d peaks shifting to lower binding energies.[42]

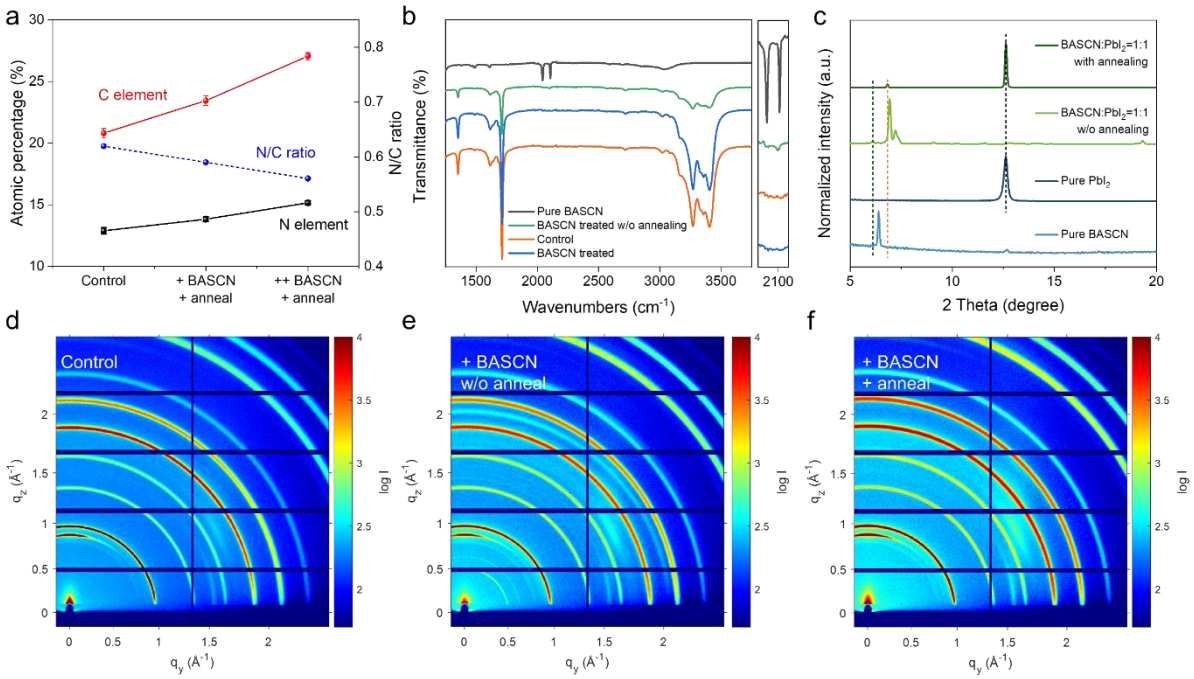

Figure 2. (a) Atomic percentages of C and N elements at the top surface of the corresponding perovskite films, extracted from XPS spectra. +BASCN and ++BASCN represent perovskite films that were treated with 2.5 mg/mL BASCN and 5 mg/mL BASCN respectively. (b) FTIR spectra of the pure BASCN film (20 mg/mL), the control perovskite film, and the BASCN (2.5 mg/mL) treated perovskite films without and with post-annealing. The figure on the right is a zoomed-in view around ~2100 cm^{-1}. (c) XRD patterns of the pure BASCN (20 mg/mL),

pure PbI_2, and BASCN:PbI_2 = 1:1 (with and without post-annealing) films. GIWAXS patterns of (d) the control perovskite film, (e) the BASCN treated perovskite film without post-annealing and (f) the BASCN treated perovskite film with post-annealing, respectively. The incidence angle is 1.294°. The perovskite is $Cs_{0.1}FA_{0.9}Pb(I_{0.9}Br_{0.1})_3$ with 2.75 mol% $PbCl_2$ as additive, and the concentration of BASCN is 2.5 mg/mL.

To detect whether SCN^- anions remain in the film, we obtained XPS spectra of S 2p for the pure BASCN and the perovskite films with BASCN treatment (**Figure S1f**). A weak peak located at ~163.5 eV for BASCN on ITO is assigned to SCN^-, while no sulfur was detected in any of the perovskite films, no matter whether they were post-annealed or not. Fourier-transform infrared spectroscopy (FTIR) spectra were also acquired to further study the presence of SCN^- anions (**Figure 2b**). The characteristic peak located at ~2100 cm^{-1} can be assigned to SCN^- vibrations, according to a previous study.[43] By simply introducing BASCN without applying post-annealing, weaker peaks are still observed. However, after post-annealing, these IR peaks cannot be observed anymore. Possible reasons for this phenomenon are: (1) SCN^- ions form volatiles with FA^+ ions, as discussed above, and thus escape from the perovskite films; (2) In XPS study, the trace amount of SCN^- is below the detection limit, which is similar to the case of Cl^- from the $PbCl_2$ that was used as additive in this work. But in all cases we cannot detect any Cl 2p peaks in XPS (**Figure S1c**).
In order to prove the interaction between Pb^{2+} and BASCN, XRD patterns of pure BASCN, pure PbI_2 and their equimolar mixtures were studied (**Figure 2c**). The main diffraction peaks of pure BASCN and PbI_2 are located at 6.4° and 12.6°, respectively. Strikingly, the mixture film without post-annealing exhibits several new peaks including a main peak at 6.9°, a sub peak at 7.2° and a very weak peak at 6.1°. In addition, no characteristic peaks belonging to PbI_2 and BASCN are detected under this condition. This suggests that a strong interaction occurred, consuming all the BASCN and PbI_2 and forming intermediate phases. However, after the post-annealing, we observed again the characteristic peak of PbI_2, located at 12.6°, accompanied by a weak peak located at 6.8°. This phenomenon indicates that the intermediate phase formed is subject to dissociation due to thermal instability, leaving another adduct in the film. Since some PbI_2 residue is left in the perovskite, as evidenced by XRD (**Figure 1e**), this intermediate phase formation will also take place during the perovskite film preparation. Therefore, through the XPS and XRD studies, we have proven that a strong interaction exists between the BASCN and Pb^{2+}.

To further investigate the perovskite surface changes upon the BASCN treatment, grazing-incidence wide-angle X-ray scattering (GIWAXS) study was performed. In **Figure 2d**, for the control sample, the main perovskite diffraction ring is located at q = ~1 $Å^{-1}$, while the ring at ~0.9 $Å^{-1}$ is attributed to the residue PbI_2 (**Figure S2**).[44] Interestingly, for the BASCN treated sample without post-annealing (**Figure 2e**), extra signals located at ~0.5 $Å^{-1}$ and ~2 $Å^{-1}$ show up, indicating that BASCN induces intermediate phases on the surface due to its strong interaction with the perovskite. Notably, these additional signals are still ring-like rather than dot-like. Dot-like signals are characteristic for 2D perovskites due to its highly ordered layered structure.[45] This means that no pure 2D perovskite was formed on the surface after the BASCN treatment. However, these additional signals vanish after post-annealing, and the diffraction pattern remains similar to the control perovskite film but with higher intensity, indicating the reconstruction process proposed above takes place (**Figure 2f**). The GIWAXS analysis agrees well with the increased crystallinity of the BASCN treated perovskite as observed by SEM.

Ultraviolet photoelectron spectroscopy (UPS) was then employed to study the energy level changes after the BASCN treatment. The corresponding UPS spectra and the schematic band diagram of the energy levels of the control and the BASCN treated perovskite films are shown in **Figure S3**. With the BASCN treatment, the Fermi level (E_F) shifts slightly upward from the initial -4.46 eV to -4.35 eV, thus a slightly more n-type perovskite was obtained after the BASCN treatment, forming an n-n isotype heterojunction between the bulk perovskite and the BASCN modified surface. This would enable a suitable band bending and better energy level alignment, which are beneficial for charge transfer and the V_{oc} improvement.[21,46]

The device performance of the gas quenched inverted PSCs was evaluated using a configuration of ITO/PTAA/perovskite/LiF/C_{60}/BCP/Cu (**Figure 3a**). 2.0 mg/mL of BASCN is selected for the BASCN treatment based on a concentration screening experiment (**Figure S4**). **Figure 3b** shows the photovoltaic parameters of the control and the BASCN treated PSCs based on $Cs_{0.1}FA_{0.9}Pb(I_{0.9}Br_{0.1})_3$ with 2.75 mol% $PbCl_2$ as additive. With the BASCN treatment, the average J_{sc} and V_{oc} increase by ~ 1 mA cm^{-2} and 35 mV, respectively, while the average FF drops slightly from 78.4% to 77.1%. The average PCE is enhanced from 17.7% to 19.0%. However, when increasing the measurement step delay time from 0.01 s to 0.1 s, an obvious drop in J_{sc} is observed for the control PSC (**Figure S5a**). In contrast, after the BASCN treatment, the J_{sc} is largely maintained at longer delay time (**Figure S5b**). Meanwhile, the hysteresis index (($PCE_{reverse}$ - $PCE_{forward}$)/$PCE_{reverse}$) is reduced from 3.3% for the control device to 2.3% for the BASCN treated device, as shown in **Figure 3c**. The

parameters are summarized in **Table S3**. Better maintained J_{sc} and the alleviation of the hysteresis indicate a reduction in the number of perovskite defects after the BASCN treatment. In addition, the maximum power point (MPP) tracking PCE increases from 17.0% to 18.4% after the BASCN treatment (**Figure 3d**). We performed a long-term moisture stability test under relative humidity of 10%-30% (**Figure 3e**). T_{80} (i.e., the efficiency drops to 80% relative to its initial value) lifetime is improved from the initial ~840 h to 2300 h. The BA^+ ions present on the surface, which contain a benzene ring with hydrophobic properties, are able to form protective sites on the surface thus enhancing the moisture stability of the treated PSCs. The thermal stability of the PSCs was also evaluated under 85 °C heating in a N_2-filled glovebox (**Figure 3f**). Inorganic metal oxides were used to replace the BCP and Cu electrodes to exclude other uncertainties such as the degradation of BCP layer. In this way we can focus on the stability of the perovskite itself. After ~1300 h of thermal ageing, the BASCN treated PSCs perform averagely ~10% better than the control PSCs, which is attributed to the better quality of BASCN treated perovskite films.

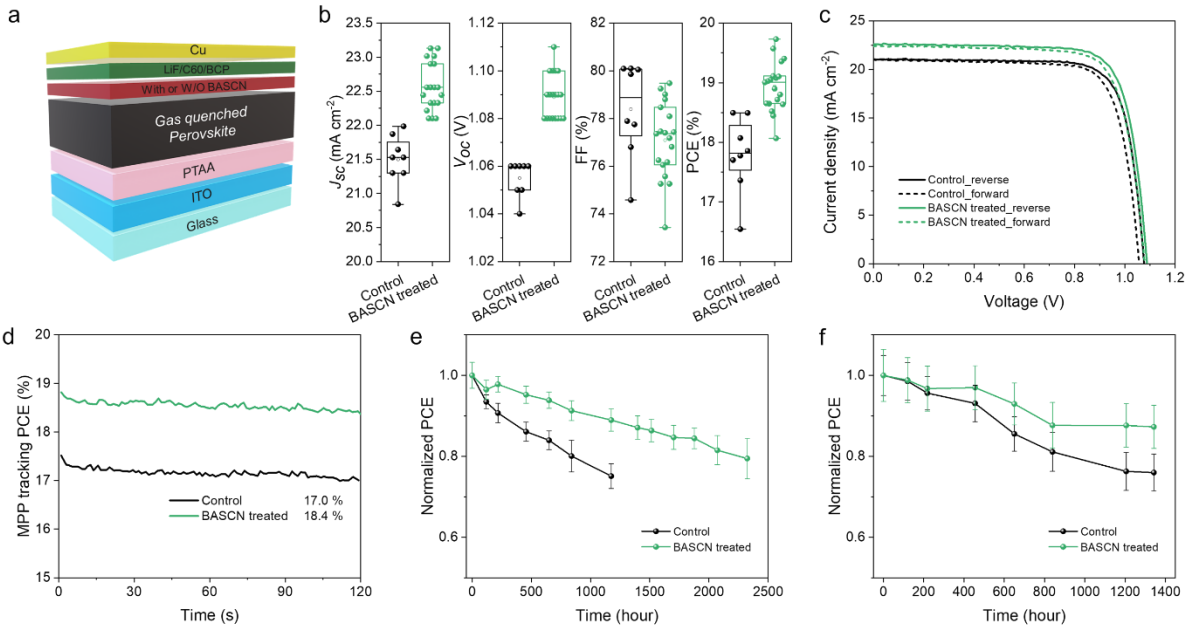

Figure 3. Device performance of the control and the BASCN treated PSCs based on $Cs_{0.1}FA_{0.9}Pb(I_{0.9}Br_{0.1})_3$ with 2.75 mol% $PbCl_2$ as additive. The concentration of BASCN is 2.0 mg/mL. (a) The schematic configuration of the gas-quenched inverted PSC devices. (b) Statistics on J_{sc}, V_{oc}, FF and PCE of the corresponding devices. The measurement delay time is 0.01 s. (c) Forward and reverse *J-V* curves and (d) MPP tracking performance of the corresponding PSCs. Stability tests of the PSCs with and without BASCN treatment. (e) Moisture stability test under relative humidity of 10%-30%. The device structure is ITO/PTAA/perovskite/LiF/C_{60}/BCP/Cu. 7 and 9 samples without encapsulation were tracked

for the control and the BASCN treated PSCs, respectively. (f) Thermal stability test under 85°C in N_2. The device structure is ITO/PTAA/perovskite/LiF/C_{60}/SnO_2/ITO. 15 and 20 samples without encapsulation were counted for the control and the BASCN treated PSCs, respectively.

In addition, gas-quenched inverted PSCs were also fabricated with a lower bandgap perovskite (1.58 eV), namely $Cs_{0.1}FA_{0.9}Pb(I_{0.955}Br_{0.045})_3$ with 2.75 mol% $PbCl_2$ as additive to confirm the universal nature of the BASCN treatment. The same phenomena are observed again on BASCN treatment, including the enhanced J_{sc} and V_{oc} (**Figure S6a**), the reduced device hysteresis index from the initial 5.0% to 4.1% (**Figure S6b** and **Table S4**), the improved MPP tracking PCE from 18.3% to 19.4% (**Figure S6c**), and a small J_{sc} drop when using 0.1 s of delay time compared to 0.01 s delay (**Figure S7**). However, from the cross-sectional SEM image (**Figure S8**), we note that the lower band-gap perovskite film is still composed of multiple grains stacking on each other in the longitudinal direction, and we assume that the BASCN treatment does not affect the grain growth in the vertical direction, as revealed before.

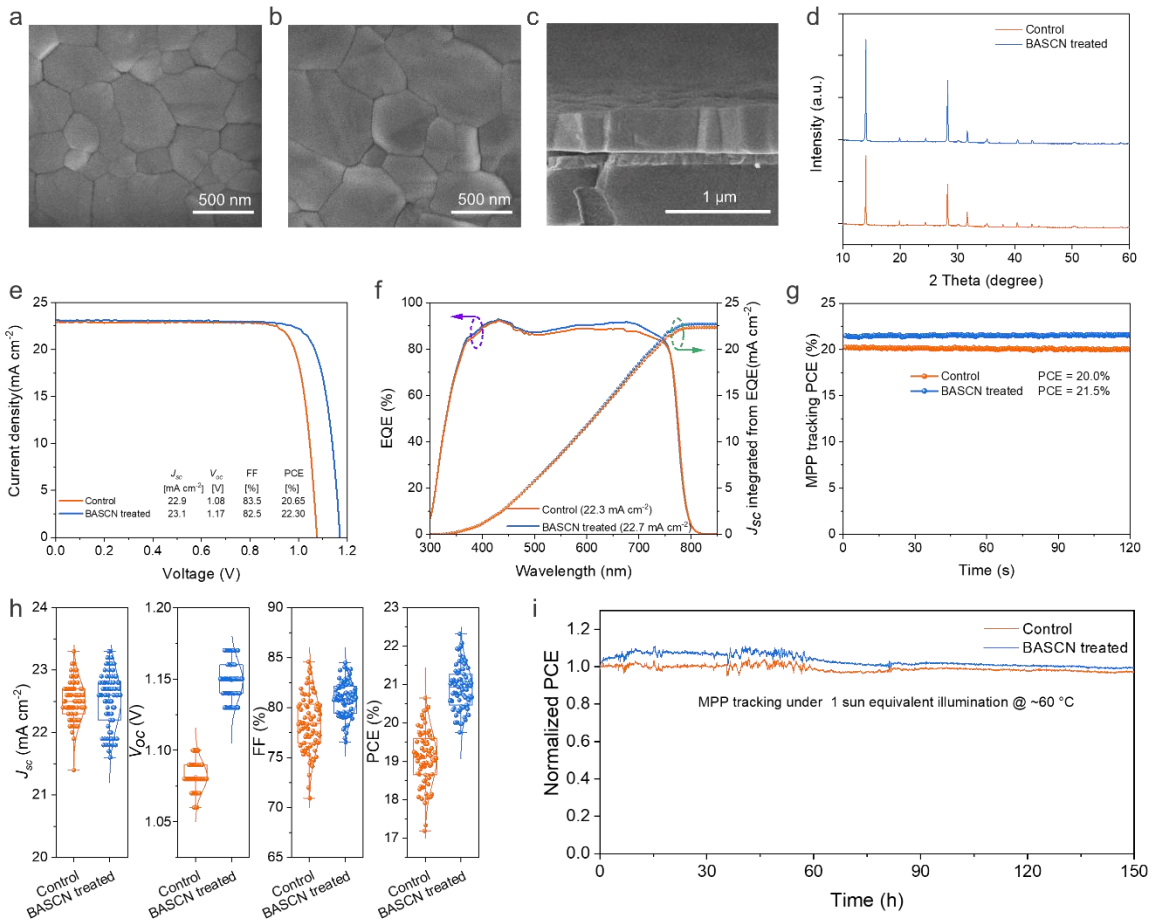

Figure 4. Morphology and device performance of the control and the BASCN treated PSCs based on $Cs_{0.1}FA_{0.9}Pb(I_{0.9}Br_{0.1})_3$ with 30 mol% MACl as additive. The concentration of BASCN is 2.0 mg/mL. Top-view SEM images of (a) the control and (b) the BASCN treated perovskite films. (c) Cross-sectional SEM image of the BASCN treated perovskite film. (d) XRD patterns of the control and the BASCN treated perovskite films. (e) *J-V* curves of the best control and the BASCN treated PSCs under reverse scan with a delay time of 0.01 s. The device structure is MgF_2/ITO/PTAA/perovskite /LiF/C_{60}/BCP/Cu (f) The corresponding EQE spectra and the integrated J_{sc}. (g) MPP tracking PCE of the corresponding PSCs. (h) The statistical photovoltaic parameters (among 75 devices), and (i) the operational stability test of the control and the BASCN treated PSCs.

The existence of longitudinally multiple grains in our gas-quenched perovskite films is consistent with literature. It is often reported that the average grain size of gas-quenched perovskite films is much smaller than that of perovskite films made by the anti-solvent method where monolithic perovskite grains are often achieved. Meanwhile, it is also observed that enhanced efficiencies are often accompanied by an increase in perovskite grain size, regardless of the method used to prepare the perovskite films.[47–50] Therefore, we believe it is essential to increase the grain size of gas-quenched perovskite films in order to further boost the device performance. Indeed, Brinkmann et al. have reported that using thiourea as the additive to increase the grain size of gas-quenched films can bring the PCE of the corresponding p-i-n PSCs to 18.5%.[51] Therefore, based on these observations and reasoning, we believe in order to further improve the device performance, it is essential to achieve gas-quenched perovskite films with monolithic grains. We accomplish this by the addition of methylammonium chloride (MACl) during film formation, an additive that has been used to tune the perovskite crystallization process successfully.[4,39,52] The top view images of the control (**Figure 4a)** and the BASCN treated (**Figure 4b**) perovskite films with MACl additive indicates that the BASCN surface treatment has a similar effect, leading to the slightly enlarged grains. However, in this case, monolithic perovskite grains are evidenced by the cross-sectional SEM image (**Figure 4c**), compared to what is shown in **Figure 1d**. XRD patterns of the control and the BASCN treated perovskite films with MACl additive show that the perovskite crystallinity can be enhanced by the BASCN treatment (**Figure 4d**). In addition, we performed XRD on the as-prepared perovskite films with different additives. As shown in **Figure S9**, the peak located at ~9.4° is assigned to the PbI_2·NMP adduct for both conditions.[53] There is no obvious perovskite peak can be found for the intermediate phase

when $PbCl_2$ is used as additive. While for the intermediate phase prepared with MACl additive, two obvious peaks belonging to (001) and (002) planes of perovskite can be found, indicating that MACl can facilitate perovskite crystallization.

PSCs with the same device configuration as previously mentioned in **Figure 3a** were fabricated to evaluate the performance of perovskite films fabricated with MACl additive. In these cells, a 100 nm thick MgF_2 anti-reflection coating was thermally evaporated onto the glass at the light incident side. **Figure 4e** illustrates the *J-V* characteristics of the control and the BASCN treated champion devices. The control device shows a PCE of 20.65% with a V_{oc} of 1.08 V, a J_{sc} of 22.9 mA cm^{-2}, and a FF of 83.5%. The BASCN treated champion device exhibits a V_{oc} of 1.17 V, a J_{sc} of 23.1 mA cm^{-2}, and an FF of 82.5%, delivering an excellent PCE of 22.30%. External quantum efficiency (EQE) measurements were performed under short-circuit without bias light on the champion PSCs and the results are presented in **Figure 4f**. Apparent enhancement of EQE can be found in the wavelength region of 500-750 nm, resulting in a slightly higher integrated J_{sc} of 22.7 mA cm^{-2} for the BASCN treated device with respect to 22.3 mA cm^{-2} for the control device. The discrepancy between the integrated J_{sc} from EQE and the values from *J-V* scan is within an acceptable range of about ~0.6 mA cm^{-2} for the control device and ~0.4 mA cm^{-2} for the BASCN treated device, respectively. As shown in **Figure 4g**, after tracking for 120 s, the BASCN treated PSC shows a stabilized PCE of 21.5%, while the control PSC reaches a PCE of 20.0%. The hysteresis index is also reduced from 2.4% to 1.4% after the BASCN treatment, as shown in **Figure S10**. In addition, the statistical distribution of the photovoltaic parameters extracted from 75 cells of each series are shown in **Figure 4h**, and the detailed average values are listed in **Table S5**. An obvious enhancement in V_{oc} from the initial average 1.08 V to 1.15 V after the BASCN treatment is demonstrated, resulting in the PCE gain from the initial average 19.1% to 20.9%. Notably, the devices with MACl additive shows better average FF compared to the ones with $PbCl_2$ additives, due to the better charge transport resulted from the formation of monolithic perovskite grains in the longitudinal direction. However, the BASCN surface treatment seems to have little influence on FF. FF changes only slightly before and after treatment, with a controversial trend for devices with $PbCl_2$ and MACl additives. In addition, the operational stability tests of the control and the BASCN treated PSCs at MPP tracking under 1 sun with a substrate temperature of ~60 °C were performed. Sputtered zinc oxide was used to replace the BCP to exclude uncertainties caused by possible degradation of BCP under thermal ageing. As shown in **Figure 4i**, both the control and the BASCN treated devices show negligible degradation after 150 h MPP tracking in a nitrogen atmosphere at a temperature of ~60 °C

under simulated 1 sun illumination, showing excellent operational stability of our gas quenched inverted PSCs.

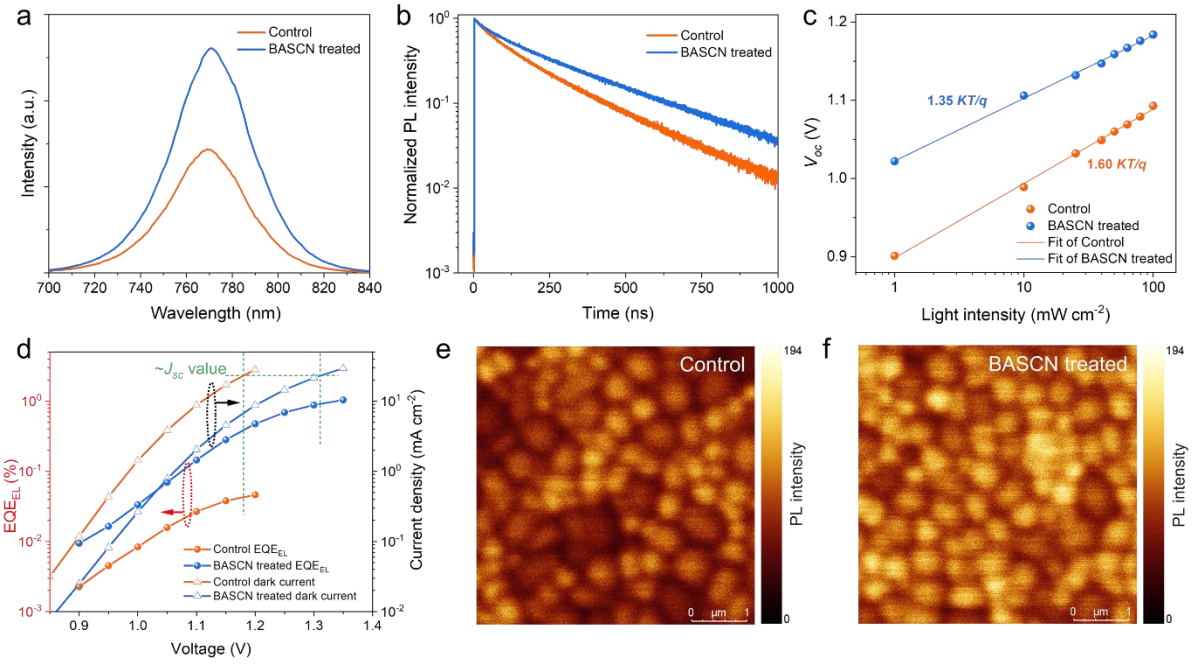

Figure 5. (a) SSPL and (b) TRPL spectra of the control and the BASCN treated perovskite films deposited on bare glass substrates. (c) Light intensity dependent *Voc* curve and (d) EQE_{EL} measurements of the control and the BASCN treated PSCs. Confocal PL mapping images of (e) the control and (f) the BASCN treated perovskite films deposited on bare glass substrates (scale bars: 1 μm). The perovskite is $Cs_{0.1}FA_{0.9}Pb(I_{0.9}Br_{0.1})_3$ with 30 mol% MACl as additive.

It is worth noting that with the BASCN treatment, the performance enhancement mainly originates from the increase in V_{oc}. Defects related characterizations were performed to understand the V_{oc} enhancement. Higher SSPL intensity and longer carrier lifetime both indicate that the recombination centers are reduced by the BASCN treatment (**Figure 5a and b**). Light intensity dependent V_{oc} and J_{sc} measurements were then conducted based on the champion control and the BASCN treated PSCs. A linear relationship with a slope of about 0.95 between the light intensity and J_{sc} for both cases suggest the bimolecular recombination can be neglected (**Figure S11a**).[39] A semi-logarithmic plot of the light intensity dependent V_{oc} is shown in **Figure 5c**, where ideality factor (n) can be obtained through fitting the V_{oc} values with a slope of nkT/q, where k is the Boltzmann's constant, T is the temperature in Kelvin, and q is the elementary charge. The n decreases from the initial 1.60 for the control PSC to 1.35 for the BASCN treated PSC, indicating a reduction in trap-assisted recombination. The detailed *J-V* responses and photovoltaic parameters are summarized in

Figure S11b and **c**, and **Table S6**, respectively. In order to qualitatively investigate the V_{oc} loss resulted from the nonradiative recombination, EQE of electroluminescence (EQE_{EL}) was performed and the results are displayed in **Figure 5d**. The EQE_{EL} of the control PSC is 0.041%, whereas it is 0.92% for the BASCN treated PSC, which is 20 times higher. Based on the following equation (1):[54]

$$V_{oc\ loss} = \frac{kT}{q} \ln\left(\frac{1}{EQE_{EL}}\right) \qquad (1)$$

the V_{oc} loss is reduced from 201 mV to 121 mV after the BASCN treatment, indicating effective passivation of the non-radiative recombination centers. In addition, hole-only devices were prepared to evaluate the trap density of the control and BASCN treated perovskite films based on the pulsed space-charge limited current measurements (**Figure S12**).[55] The pulsed length is 100 ms. According to the equation of $N_t = 2\varepsilon_0\varepsilon V_{TFL}/eL^2$, where ε_0 is the vacuum permittivity, ε is the relative dielectric constant of perovskite, e is the electron charge and L is the perovskite thickness, the trap density is reduced from the initial 3.94×10^{16} to 2.34×10^{16} after the BASCN treatment, which aslo confirms the passivation of defects. Confocal PL mapping was further performed to study the uniformity of the perovskite films as shown in **Figure 5e** and **f**. More homogeneous films with enhanced PL intensity are obtained with the BASCN treatment, significantly facilitating the charge transfer.[52] Finally, much higher PL intensities are measured within the grains than at the grain boundaries. Furthermore, this integrated strategy of MACl additive and BASCN surface treatment was applied in gas quenched large-area devices, i.e. 1 cm^2 PSC and 4 cm^2 perovskite mini-module. **Figure S13** shows the photograph and device performance of the corresponding devices. Specifically, with the combined modifications, the 1 cm^2 PSC shows a PCE of 20.0% and the 4 cm^2 perovskite mini-module shows an active area PCE of 18.5%.

3. Conclusion

In summary, we have demonstrated the application of an integrated strategy for perovskite bulk and surface modification in gas quenched inverted p-i-n PSCs. The application of BASCN as surface modifier induces recrystallization of perovskite, formation of larger grains, and passivates defects effectively, while the introduction of MACl improves the perovskite crystallinity and results in monolithic perovskite grains. The application of the integrated modification strategy leads to an increased average V_{oc} of our gas-quenched inverted PSCs from 1.08 V to 1.15 V, and an improved average PCE from 19.1% to 20.9%. A champion PCE of 22.3% for the gas-quenched PSCs is obtained with a perovskite composition of $Cs_{0.1}FA_{0.9}Pb(I_{0.9}Br_{0.1})_3$. With this integrated strategy, the 1 cm^2 PSC shows a PCE of 20.0%

and the 4 cm^2 perovskite mini-module shows an active area PCE of 18.5%. Moreover, enhanced moisture stability, thermal stability and excellent operational stability were demonstrated, representing an important step forward for gas-quenched inverted p-i-n PSCs.

Supporting Information
Supporting Information is available from the Wiley Online Library or from the author.

Acknowledgements
X.Z and W. Q contributed equally to this work. This work has received funding from the European Union's Horizon 2020 research and innovation programme under grant agreement No. 850937 of the PERCISTAND project, the FLAG-ERA JTC 2019 programme under Reference Number of JTC-2019-013 of the LASERGRAPH project, and the funding from the European Union's H2020 Programme for research, technological development and demonstration under grant agreement No. 764047 of the ESPResSo project. This work was also partially supported by the Kuwait Foundation for the Advancement of Sciences under the grant number CN18-15EE-01. Funding from the Swedish Energy Council for the project PERDRY (grant No. 48381-1) within the framework of SOLAR-ERA.NET Cofund 2 is also acknowledged. We are also thankful for the funding received from the EU-H2020 Research and Innovation Programme under grant agreement no. 654360 having benefitted from access to the Austrian SAXS beamline provided by TUG@Elettra in Trieste, Italy, within the framework of the NFFA-Europe Transnational Access Activity. In addition, X.Z. thanks the China Association for Science and Technology (CAST) for the support from 2020 Youth Exchange project. W.Q. would like to thank the financial support of the postdoctoral fellowship grant from FWO. B. P. acknowledges a postdoctoral fellowship from the Research Foundation-Flanders (FWO Grant No. 1275521N). Y.Zhan acknowledges financial support from the National Natural Science Foundation of China under the grant number of 61776046. J.H. gratefully acknowledges financial support from the Research Foundation - Flanders (FWO Grant Numbers S002019N, 1514220N, G.0B39.15, G.0B49.15, G098319N, and ZW15 09-GOH6316), the KU Leuven Research Fund (iBOF-21-085 PERSIST) and the Flemish government through long term structural funding Methusalem (CASAS2, Meth/15/04).

Conflict of Interest

A patenting process is pending.

Received: ((will be filled in by the editorial staff))
Revised: ((will be filled in by the editorial staff))
Published online: ((will be filled in by the editorial staff))

References

[1] M. Saliba, T. Matsui, J.-Y. Seo, K. Domanski, J.-P. Correa-Baena, M. K. Nazeeruddin, S. M. Zakeeruddin, W. Tress, A. Abate, A. Hagfeldt, M. Grätzel, *Energy Environ. Sci.* **2016**, *9*, 1989.
[2] T. Bu, X. Liu, Y. Zhou, J. Yi, X. Huang, L. Luo, J. Xiao, Z. Ku, Y. Peng, F. Huang, Y.-B. Cheng, J. Zhong, *Energy Environ. Sci.* **2017**, *10*, 2509.
[3] S.-H. Turren-Cruz, A. Hagfeldt, M. Saliba, *Science* **2018**, *362*, 449.
[4] J. Jeong, M. Kim, J. Seo, H. Lu, P. Ahlawat, A. Mishra, Y. Yang, M. A. Hope, F. T. Eickemeyer, M. Kim, Y. J. Yoon, I. W. Choi, B. P. Darwich, S. J. Choi, Y. Jo, J. H. Lee, B. Walker, S. M. Zakeeruddin, L. Emsley, U. Rothlisberger, A. Hagfeldt, D. S. Kim, M. Grätzel, J. Y. Kim, *Nature* **2021**, *592*, 381.
[5] S. Yang, S. Chen, E. Mosconi, Y. Fang, X. Xiao, C. Wang, Y. Zhou, Z. Yu, J. Zhao, Y. Gao, F. De Angelis, J. Huang, *Science* **2019**, *365*, 473.
[6] J. Peng, D. Walter, Y. Ren, M. Tebyetekerwa, Y. Wu, T. Duong, Q. Lin, J. Li, T. Lu, M. A. Mahmud, O. L. C. Lem, S. Zhao, W. Liu, Y. Liu, H. Shen, L. Li, F. Kremer, H. T. Nguyen, D.-Y. Choi, K. J. Weber, K. R. Catchpole, T. P. White, *Science* **2021**, *371*, 390.
[7] A. Al-Ashouri, A. Magomedov, M. Roß, M. Jošt, M. Talaikis, G. Chistiakova, T. Bertram, J. A. Márquez, E. Köhnen, E. Kasparavičius, S. Levcenco, L. Gil-Escrig, C. J. Hages, R. Schlatmann, B. Rech, T. Malinauskas, T. Unold, C. A. Kaufmann, L. Korte, G. Niaura, V. Getautis, S. Albrecht, *Energy Environ. Sci.* **2019**, *12*, 3356.
[8] E. Aktas, N. Phung, H. Köbler, D. A. González, M. Méndez, I. Kafedjiska, S.-H. Turren-Cruz, R. Wenisch, I. Lauermann, A. Abate, E. Palomares, *Energy Environ. Sci.* **2021**, *14*, 3976.
[9] Z. Dai, S. K. Yadavalli, M. Chen, A. Abbaspourtamijani, Y. Qi, N. P. Padture, *Science* **2021**, *372*, 618.
[10] T. Zhang, Z. Cao, Y. Shang, C. Cui, P. Fu, X. Jiang, F. Wang, K. Xu, D. Yin, D. Qu, Z. Ning, *J. Photochem. Photobiol. A Chem.* **2018**, *355*, 42.
[11] J. V. Milić, D. J. Kubicki, L. Emsley, M. Grätzel, *Chimia* **2019**, *73*, 317.
[12] X. Yu, Y. Lv, B. Xue, L. Wang, W. Hu, X. Liu, S. Yang, W.-H. Zhang, *Nano Energy* **2022**, *93*, 106856.
[13] J. Yang, W. Tang, R. Yuan, Y. Chen, J. Wang, Y. Wu, W.-J. Yin, N. Yuan, J. Ding, W.-H. Zhang, *Chem. Sci.* **2021**, *12*, 2050.
[14] A. Mei, Y. Sheng, Y. Ming, Y. Hu, Y. Rong, W. Zhang, S. Luo, G. Na, C. Tian, X. Hou, Y. Xiong, Z. Zhang, S. Liu, S. Uchida, T.-W. Kim, Y. Yuan, L. Zhang, Y. Zhou, H. Han, *Joule* **2020**, *4*, 2646.
[15] N. J. Jeon, J. H. Noh, Y. C. Kim, W. S. Yang, S. Ryu, S. Il Seok, *Nat. Mater.* **2014**, *13*, 897.
[16] Q. Jiang, Z. Chu, P. Wang, X. Yang, H. Liu, Y. Wang, Z. Yin, J. Wu, X. Zhang, J. You, *Adv. Mater.* **2017**, *29*, 1703852.
[17] X. Li, D. Bi, C. Yi, J.-D. Décoppet, J. Luo, S. M. Zakeeruddin, A. Hagfeldt, M. Grätzel, *Science* **2016**, *353*, 58.
[18] B. Conings, A. Babayigit, M. Klug, S. Bai, N. Gauquelin, N. Sakai, J. T.-W. Wang, J.

Verbeeck, H.-G. Boyen, H. Snaith, *2018 IEEE 7th World Conf. Photovolt. Energy Convers.* **2018**, 1724.
[19] M. Liu, M. B. Johnston, H. J. Snaith, *Nature* **2013**, *501*, 395.
[20] S. Wu, J. Zhang, Z. Li, D. Liu, M. Qin, S. H. Cheung, X. Lu, D. Lei, S. K. So, Z. Zhu, A. K.-Y. Jen, *Joule* **2020**, *4*, 1248.
[21] Y.-N. Lu, J.-X. Zhong, Y. Yu, X. Chen, C.-Y. Yao, C. Zhang, M. Yang, W. Feng, Y. Jiang, Y. Tan, L. Gong, X. Wei, Y. Zhou, L. Wang, W.-Q. Wu, *Energy Environ. Sci.* **2021**, *14*, 4048.
[22] X. Zheng, Y. Hou, C. Bao, J. Yin, F. Yuan, Z. Huang, K. Song, J. Liu, J. Troughton, N. Gasparini, C. Zhou, Y. Lin, D.-J. Xue, B. Chen, A. K. Johnston, N. Wei, M. N. Hedhili, M. Wei, A. Y. Alsalloum, P. Maity, B. Turedi, C. Yang, D. Baran, T. D. Anthopoulos, Y. Han, Z.-H. Lu, O. F. Mohammed, F. Gao, E. H. Sargent, O. M. Bakr, *Nat. Energy* **2020**, *5*, 131.
[23] X. Hu, C. Liu, Z. Zhang, X.-F. Jiang, J. Garcia, C. Sheehan, L. Shui, S. Priya, G. Zhou, S. Zhang, K. Wang, *Adv. Sci.* **2020**, *7*, 2001285.
[24] M. Zhang, J. Bing, Y. Cho, Y. Li, J. Zheng, C. F. J. Lau, M. A. Green, S. Huang, A. W. Y. Ho-Baillie, *Nano Energy* **2019**, *63*, 103853.
[25] M. Zhang, B. Wilkinson, Y. Liao, J. Zheng, C. F. J. Lau, J. Kim, J. Bing, M. A. Green, S. Huang, A. W.-Y. Ho-Baillie, *Joule* **2018**, *2*, 2694.
[26] M. Du, X. Zhu, L. Wang, H. Wang, J. Feng, X. Jiang, Y. Cao, Y. Sun, L. Duan, Y. Jiao, K. Wang, X. Ren, Z. Yan, S. Pang, S. (Frank) Liu, *Adv. Mater.* **2020**, *32*, 2004979.
[27] S. Tang, J. Bing, J. Zheng, J. Tang, Y. Li, M. Mayyas, Y. Cho, T. W. Jones, T. C.-J. Yang, L. Yuan, M. Tebyetekerwa, H. T. Nguyen, M. P. Nielsen, N. J. Ekins-Daukes, K. Kalantar-Zadeh, G. J. Wilson, D. R. McKenzie, S. Huang, A. W. Y. Ho-Baillie, *Cell Reports Phys. Sci.* **2021**, 100511.
[28] K. Liu, Q. Liang, M. Qin, D. Shen, H. Yin, Z. Ren, Y. Zhang, H. Zhang, P. W. K. Fong, Z. Wu, J. Huang, J. Hao, Z. Zheng, S. K. So, C.-S. Lee, X. Lu, G. Li, *Joule* **2020**, *4*, 2404.
[29] S. Chen, X. Dai, S. Xu, H. Jiao, L. Zhao, J. Huang, *Science* **2021**, *373*, 902.
[30] S. Wang, A. Wang, X. Deng, L. Xie, A. Xiao, C. Li, Y. Xiang, T. Li, L. Ding, F. Hao, *J. Mater. Chem. A* **2020**, *8*, 12201.
[31] S. Ghosh, T. Singh, *Nano Energy* **2019**, *63*, 103828.
[32] J. Yuan, Y. Jiang, T. He, G. Shi, Z. Fan, M. Yuan, *Sci. China Chem.* **2019**, *62*, 629.
[33] H. Zheng, G. Liu, L. Zhu, J. Ye, X. Zhang, A. Alsaedi, T. Hayat, X. Pan, S. Dai, *Adv. Energy Mater.* **2018**, *8*, 1800051.
[34] L. Gao, I. Spanopoulos, W. Ke, S. Huang, I. Hadar, L. Chen, X. Li, G. Yang, M. G. Kanatzidis, *ACS Energy Lett.* **2019**, *4*, 1763.
[35] S. Gharibzadeh, P. Fassl, I. Hossain, P. N. Rohrbeck, M. Frericks, M. Schmidt, T. Duong, M. R. Khan, T. Abzieher, B. Abdollahi Nejand, F. Schackmar, O. Almora, T. Feeney, R. Singh, D. Fuchs, U. Lemmer, J. P. Hofmann, S. Weber, U. W. Paetzold, *Energy Environ. Sci.* **2021**, DOI: 10.1039/D1EE01508G.
[36] C. Ran, J. Xu, W. Gao, C. Huang, S. Dou, *Chem. Soc. Rev.* **2018**, *47*, 4581.
[37] N. Zhou, Y. Shen, Y. Zhang, Z. Xu, G. Zheng, L. Li, Q. Chen, H. Zhou, *Small* **2017**, *13*, 1700484.
[38] X. Zheng, Y. Hou, C. Bao, J. Yin, F. Yuan, Z. Huang, K. Song, J. Liu, J. Troughton, N. Gasparini, C. Zhou, Y. Lin, D.-J. Xue, B. Chen, A. K. Johnston, N. Wei, M. N. Hedhili, M. Wei, A. Y. Alsalloum, P. Maity, B. Turedi, C. Yang, D. Baran, T. D. Anthopoulos, Y. Han, Z.-H. Lu, O. F. Mohammed, F. Gao, E. H. Sargent, O. M. Bakr, *Nat. Energy* **2020**, *5*, 131.
[39] H. Lu, Y. Liu, P. Ahlawat, A. Mishra, W. R. Tress, F. T. Eickemeyer, Y. Yang, F. Fu,

Z. Wang, C. E. Avalos, B. I. Carlsen, A. Agarwalla, X. Zhang, X. Li, Y. Zhan, S. M. Zakeeruddin, L. Emsley, U. Rothlisberger, L. Zheng, A. Hagfeldt, M. Grätzel, *Science* **2020**, *370*, eabb8985.

[40] T. Cai, F. Li, Y. Jiang, X. Liu, X. Xia, X. Wang, J. Peng, L. Wang, W. A. Daoud, *Nanoscale* **2019**, *11*, 1319.

[41] S. Tan, T. Huang, I. Yavuz, R. Wang, M. H. Weber, Y. Zhao, M. Abdelsamie, M. E. Liao, H.-C. Wang, K. Huynh, K.-H. Wei, J. Xue, F. Babbe, M. S. Goorsky, J.-W. Lee, C. M. Sutter-Fella, Y. Yang, *J. Am. Chem. Soc.* **2021**, *143*, 6781.

[42] A. Thote, I. Jeon, J.-W. Lee, S. Seo, H.-S. Lin, Y. Yang, H. Daiguji, S. Maruyama, Y. Matsuo, *ACS Appl. Energy Mater.* **2019**, *2*, 2486.

[43] F. Gao, C. Li, L. Qin, L. Zhu, X. Huang, H. Liu, L. Liang, Y. Hou, Z. Lou, Y. Hu, F. Teng, *RSC Adv.* **2018**, *8*, 14025.

[44] Y. Liu, S. Akin, A. Hinderhofer, F. T. Eickemeyer, H. Zhu, J.-Y. Seo, J. Zhang, F. Schreiber, H. Zhang, S. M. Zakeeruddin, A. Hagfeldt, M. I. Dar, M. Grätzel, *Angew. Chemie Int. Ed.* **2020**, *59*, 15688.

[45] Y.-W. Jang, S. Lee, K. M. Yeom, K. Jeong, K. Choi, M. Choi, J. H. Noh, *Nat. Energy* **2021**, *6*, 63.

[46] F. Zhang, S. Ye, H. Zhang, F. Zhou, Y. Hao, H. Cai, J. Song, J. Qu, *Nano Energy* **2021**, *89*, 106370.

[47] N. Li, X. Niu, L. Li, H. Wang, Z. Huang, Y. Zhang, Y. Chen, X. Zhang, C. Zhu, H. Zai, Y. Bai, S. Ma, H. Liu, X. Liu, Z. Guo, G. Liu, R. Fan, H. Chen, J. Wang, Y. Lun, X. Wang, J. Hong, H. Xie, D. S. Jakob, X. G. Xu, Q. Chen, H. Zhou, *Science* **2021**, *373*, 561 LP.

[48] Y. Zhao, H. Tan, H. Yuan, Z. Yang, J. Z. Fan, J. Kim, O. Voznyy, X. Gong, L. N. Quan, C. S. Tan, J. Hofkens, D. Yu, Q. Zhao, E. H. Sargent, *Nat. Commun.* **2018**, *9*, 1607.

[49] H. Li, G. Wu, W. Li, Y. Zhang, Z. Liu, D. Wang, S. (Frank) Liu, *Adv. Sci.* **2019**, *6*, 1901241.

[50] M. Kim, G.-H. Kim, T. K. Lee, I. W. Choi, H. W. Choi, Y. Jo, Y. J. Yoon, J. W. Kim, J. Lee, D. Huh, H. Lee, S. K. Kwak, J. Y. Kim, D. S. Kim, *Joule* **2019**, *3*, 2179.

[51] K. O. Brinkmann, J. He, F. Schubert, J. Malerczyk, C. Kreusel, F. van gen Hassend, S. Weber, J. Song, J. Qu, T. Riedl, *ACS Appl. Mater. Interfaces* **2019**, *11*, 40172.

[52] F. Li, X. Deng, F. Qi, Z. Li, D. Liu, D. Shen, M. Qin, S. Wu, F. Lin, S.-H. Jang, J. Zhang, X. Lu, D. Lei, C.-S. Lee, Z. Zhu, A. K.-Y. Jen, *J. Am. Chem. Soc.* **2020**, *142*, 20134.

[53] B. Tongle, L. Jing, L. Hengyi, T. Congcong, S. Jie, T. Guoqing, O. L. K., W. Chao, L. Zhipeng, C. Nianyao, Z. Xiao-Li, C. Jingjing, L. Jianfeng, Z. Jie, H. Wenchao, Q. Yabing, C. Yi-Bing, H. Fuzhi, *Science* **2021**, *372*, 1327.

[54] R. Su, Z. Xu, J. Wu, D. Luo, Q. Hu, W. Yang, X. Yang, R. Zhang, H. Yu, T. P. Russell, Q. Gong, W. Zhang, R. Zhu, *Nat. Commun.* **2021**, *12*, 2479.

[55] V. M. Le Corre, E. A. Duijnstee, O. El Tambouli, J. M. Ball, H. J. Snaith, J. Lim, L. J. A. Koster, *ACS Energy Lett.* **2021**, *6*, 1087.

An integrated bulk and surface modification strategy for gas-quenched inverted perovskite solar cells with efficiencies exceeding 22%

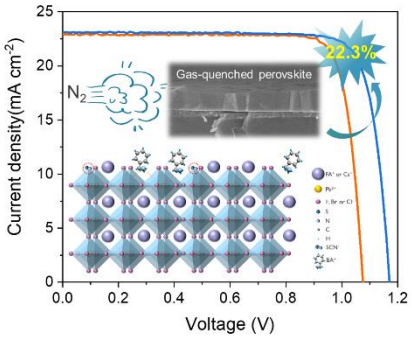

A combined application of BASCN surface modification and MACl additive engineering is applied to improve the film quality of Cs-FA double cation perovskite, helping to achieve enlarged and monolithic perovskite grains, better interfacial properties and passivate the nonradiative recombination centers. As a result, a distinguished power conversion efficiency of 22.3% is realized for gas-quenched inverted p-i-n perovskite solar cells.

Supplementary Information

An integrated bulk and surface modification strategy for gas-quenched inverted perovskite solar cells with efficiencies exceeding 22%

Xin Zhang, Weiming Qiu*, Wenya Song, Zafer Hawash, Yaxin Wang, Bapi Pradhan, Yiyue Zhang, Denys Naumenko, Heinz Amenitsch, Ellen Moons, Tamara Merckx, Aranzazu Aguirre, Yaser Abdulraheem, Tom Aernouts, Yiqiang Zhan*, Yinghuan Kuang*, Johan Hofkens, Jef Poortmans*

Methods

Materials

Indium tin oxide (ITO) coated glass substrates were purchased from Colorado Concept Coatings LLC. Poly[bis(4-phenyl)(2,4,6-trimethylphenyl)amine] (PTAA) was purchased from Xi'an p-OLED. Methylammonium chloride (MACl) was purchased from Shanghai MaterWin. Formamidinium bromide (FABr) and formamidinium iodide (FAI) and benzylammonium thiocyanate (BASCN) were purchased from Greatcell Solar Materials. Lead iodide (PbI_2) and cesium iodide (CsI) were purchased from Tokyo Chemical Industry (TCI). Lead bromide ($PbBr_2$), lead chloride ($PbCl_2$) and lithiumfluorid (LiF) were purchased from Sigma Aldrich. Fullerene C_{60} was purchased from Nano-C. 2,9-dimethyl-4,7-diphenyl-1,10-phenanthroline (BCP) and 2,2',7,7'-Tetrakis[N,N-di(4-methoxyphenyl)amino]-9,9'-spirobifluorene (Spiro-OMeTAD) were purchased from Luminescence Technology Corp. (Lumtec). Lithium bis(trifluoromethanesulfonyl)imide (Li-TFSI), 4-*tert*-Butylpyridine (4-*t*BP), acetonitrile, chlorobenzene, anhydrous dimethylformamide (DMF), anhydrous 1-methyl-2-pyrrolidone (NMP), anhydrous toluene and anhydrous isopropanol alcohol (IPA) were purchased from Sigma Aldrich. Absolute acetone and isopropanol were purchased from VWR. All materials were used as received.

Device fabrication

Indium tin oxide (ITO) coated substrates (15 Ω sq^{-1}) of 3 cm × 3 cm were ultrasonic cleaned in diluted detergent, deionized water, acetone and isopropanol for 15 minutes, respectively. Then the substrates were dried in air in a fume hood and transferred to a nitrogen-filled glove box. 2 mg/mL of PTAA dissolved in anhydrous toluene was spin-coated on the substrate at a speed of 5500 rpm. for 35 s and followed by annealing at 100 °C for 10 minutes. The double cation perovskite ($Cs_{0.1}FA_{0.9}Pb(I_{0.9}Br_{0.1})_3$) precursor was prepared by dissolving 0.135 M CsI, 1.2 M FAI, 1.2 M PbI_2 and 0.2 M $PbBr_2$ in DMF/NMP (9:1 vol:vol) mixed solvent. 2.75

mol% of $PbCl_2$ or 30 mol% of MACl was used as additive in the precursor. For the preparation of $Cs_{0.1}FA_{0.9}Pb(I_{0.955}Br_{0.045})_3$ perovskite, 1.245 M PbI_2, 0.125 M CsI, 0.952 M FAI, 0.168 M FABr and 0.034 M $PbCl_2$ were dissolved in 1 mL DMF/NMP (9:1 vol:vol) mixed solvent. The precursor solution was dynamically spin-coated on the PTAA/ITO substrates by a continuous two-step program, which is 2000 rpm. for 10 s and then 5000 rpm. for 45 seconds. During this process, the perovskite film was quenched with nitrogen for 30 s, starting at 40 seconds prior to the end. Then the perovskite films were annealed at 130 °C for 20 minutes (in case of $PbCl_2$ as additive) or annealed at 110 °C for 40 minutes (in case of MACl as additive). After cooling for 10 minutes, BASCN dissolved in anhydrous IPA was coated on the perovskite films with a speed of 3000 rpm. for 30 s and followed by a short annealing at the same temperature as used in perovskite annealing for 5 min. Afterwards, samples were transferred into a high-vacuum chamber (base pressure 10^{-7}~10^{-8} Torr) to deposit 0.8 nm of LiF (0.1 Å/s), 20 nm of C_{60} (0.5 Å/s), and 5 nm of BCP (0.5 Å/s), all by thermal evaporation. Finally, a 100 nm thick copper (Cu) layer was prepared by thermal evaporation at 2 Å/s rate. The active cell area of 0.13 cm^2 is defined by a metal mask. For the thermal stability tests, tin oxide prepared by spin-coating SnO_2 nanoparticle dispersion (Avantama, 2.5 wt% in mixture of butanols) was used to replace the BCP. ITO top electrodes were prepared by magnetron sputtering (power density of 0.3 W cm^{-2}, pressure of 2 mTorr, Ar:O_2 = 15 sccm:0.2 sccm). For the operational stability test samples, zinc oxide prepared by magnetron sputtering using Argon plasma under gentle conditions (power density of 0.18 W cm^{-2}, pressure of 3 mTorr) was used to replace the BCP. For the hole-only devices, spiro-OMeTAD was spin-coated on the substrate at a speed of 5500 rpm. for 35 s. 18.0 μL of Li-TFSI (520 mg mL^{-1} in acetonitrile) and 29.0 μL of 4-*t*BP were added to the spiro-OMeTAD solution (72.3 mg mL^{-1} in chlorobenzene). Then, 80 nm gold (Au) was prepared by thermal evaporation at 1 Å/s rate. For the perovskite module, P1, P2 and P3 were done with a pico-second laser in a glove box.

Characterizations

The current-voltage (*J-V*) characteristic was measured in an N_2 filled glove box at 30 °C, using Abet Sun 3000 solar simulator. A Keithley 2602A source meter was used to record the *I-V* of the PSCs (1 V s^{-1}, 10 mV step, 0.01 s or 0.1 s of delay time). The simulated solar irradiation of 100 mW cm^{-2} is obtained from a 450 W xenon lamp, and calibrated with a Fraunhofer ISE's WPVS reference solar cell (Type: RS-ID-4). The maximum power point tracking was recorded following our previous work, which is a dynamic tracking process.[1]

EQE was measured by the Bentham PVE300 system from 300 nm to 850 nm with a 5 nm resolution in ambient. The top-view and cross-sectional SEM images of the perovskite films were obtained by a field-emission SEM under an accelerating voltage of 5 kV (Nova 200, FEI). The XRD measurements were performed by using a Bruker-AXS D8 system with Cu Kα as the radiation source. UV-Vis absorption spectra were obtained using a UV-1601PC spectrophotometer (Shimadzu). The steady-state and transient PL measurements were performed on PicoQuant FluoTime 300 in ambient. Long-term operational stability tests were performed by a homemade system. FTIR spectra were acquired by a Fourier transform infrared spectroscopy from Bruker (IFS 66v/S) in transmittance mode. EQE_{EL} was measured by a Thorlabs integrating sphere (IS236A-4) coupled with a calibrated silicon photodiode and a Flame Spectrometer from Ocean Optics.[2] PL mapping images acquired with a confocal microscopy TCS SP8 X, 532 nm excitation source was provided by a supercontinuum laser.

Grazing-incidence wide-angle X-ray scattering (GIWAXS)

GIWAXS measurements have been performed at the Austrian SAXS beamline at the ELETTRA synchrotron (Trieste, Italy) at photon energy of 8 keV.[3] The beam size was set to 1×0.1 mm^2 (H × V). The sample to detector (Pilatus3 1M, Dectris) distance was adjusted to 217 mm calibrated with silver behenate as a reference pattern. All measurements have been performed at an incident angle of 1.294º in air with 60 s exposure time. The GIWAXS patterns have been corrected for the fluctuations of the primary intensity and processed with the GIXSGUI toolbox.[4,5]

Ultraviolet and X-ray photoelectron spectroscopy (UPS and XPS) measurements

Ultraviolet and X-ray photoelectron spectroscopy (UPS and XPS) measurements were performed in an ultra-high vacuum (UHV) system equipped with Scienta-Omicron SES-100 electron analyzer, a UV-source (He−Iα = 21.22 eV), and a non-monochromatic x-ray source (Mg−Kα = 1253.7 eV). The base pressure of the UHV system prior to UPS and XPS was about 5×10^{-11} mbar and about 5×10^{-10} mbar during XPS measurements. A pass energy of 2 eV and 20 eV were used for UPS and XPS, respectively. The electron analyzer was calibrated using a clean surface of Au sample by measuring Fermi Energy ($E_F = 0$) and Au $4f_{7/2}$ peak maximum at 84.0 eV. The x-ray gun was operated at 240 W. Possible ultraviolet or x-ray radiation damage were monitored by performing the measurements as set of consecutive scans for each core level or region. Each scan took about 2–3 minutes. In case that no changes were observed in the scans then it was averaged into one scan. The prepared samples were

also handled and transferred only in an inert atmosphere of nitrogen using UHV compatible suitcases. XPS and UPS data processing was first performed using CasaXPS 2.3.16 software followed by further processing using Origin 2018b9 software. Hartree-Slater Subshell Photoionization Cross-Sections at 1253.7 eV were used for atomic percentages and normalization calculations for each specific core level or spin-orbit splitting.[6] Shirley background subtraction was also used for XPS quantifications.[7]

Calculation method in TRPL analysis section

$$I(t) = A_1 \exp\left(-\frac{t}{\tau_1}\right) + A_2 \exp\left(-\frac{t}{\tau_2}\right) \quad \text{(S1)}$$

$$\tau_{average} = \frac{A_1\tau_1^2 + A_2\tau_2^2}{A_1\tau_1 + A_2\tau_2} \quad \text{(S2)}$$

$$\sqrt{D \times \tau} = L \approx \frac{2d}{\pi}\sqrt{2\left(\frac{\tau}{\tau'} - 1\right)} \quad \text{(S3)}$$

$$D = \mu \times k \times T/q \quad \text{(S4)}$$

Where L is diffusion length, D is diffusion coefficient, d is film thickness, τ is carrier lifetime, τ' is quenched carrier lifetime, μ, k, T *and* q represent carrier mobility, Boltzmann's constant (1.38×10^{-23} m^2 kg s^{-2} K^{-1}), temperature (300 K) and elementary charge (1.6×10^{-23} C), respectively.

Table S1. Parameters of the TRPL study based on the perovskite films deposited on bare glass.

	Control	BASCN treated
$\boldsymbol{A_1}$	0.698	0.652
$\boldsymbol{\tau_1}$	14.7	16.27
$\boldsymbol{A_2}$	0.447	0.421
$\boldsymbol{\tau_2}$	265.9	321.8
$\boldsymbol{\tau_{average}}$	245.9	299.6

Table S2. Parameters of the TRPL study based on the PCBM/perovskite films deposited on bare glass.

	Control	BASCN treated
A_1	0.775	0.968
τ_1	10.3	8.5
A_2	0.393	0.355
τ_2	64.4	51.2
$\tau_{average}$	51.4	37.9

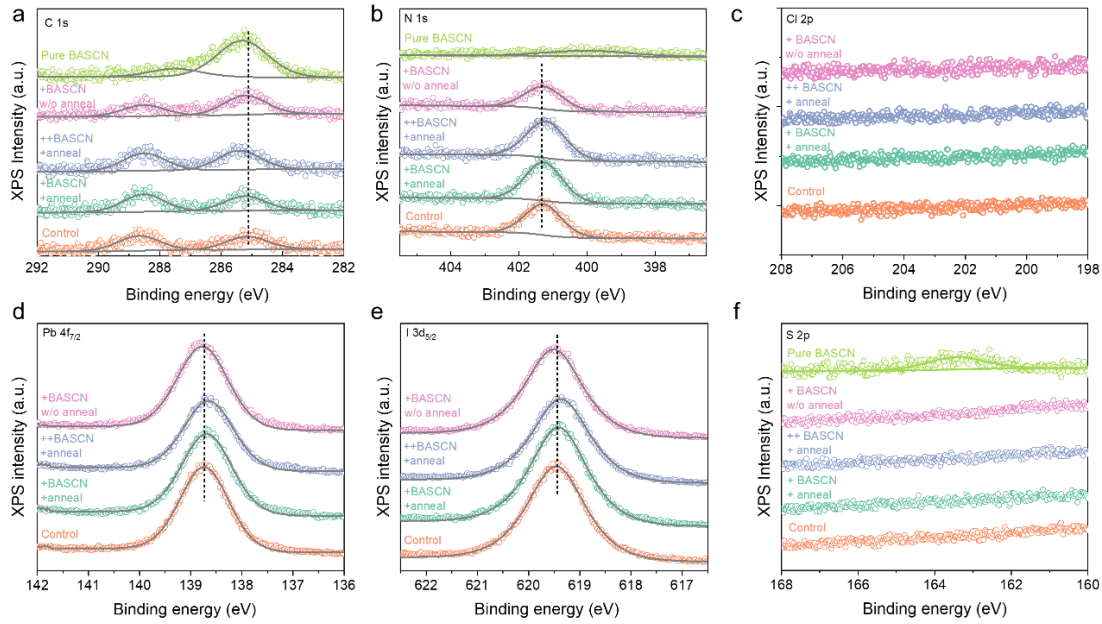

Figure S1. (a) C 1s, (b) N 1s, (c) Cl 2p, (d) Pb $4f_{7/2}$, and (e) I $3d_{5/2}$ XPS spectra of the perovskite films prepared under different conditions. The perovskite is $Cs_{0.1}FA_{0.9}Pb(I_{0.9}Br_{0.1})_3$ with 2.75 mol% $PbCl_2$ as additive. Orange circles: control perovskite. Green circles: perovskite modified with a moderate concentration of BASCN (2.5 mg/mL) and followed by post-annealing. Blue circles: perovskite modified with a high concentration of BASCN (5 mg/mL) and followed by post-annealing. Pink circles: perovskite modified with a moderate concentration of BASCN (2.5 mg/mL), but without post-annealing. Light green circles: pure BASCN film on bare ITO substrate (20 mg/mL).

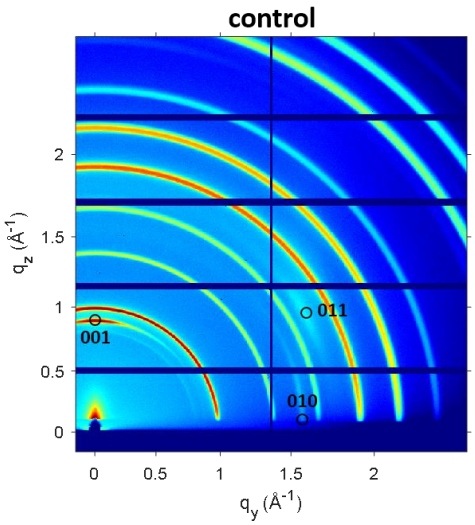

Figure S2. GIWAXS pattern of the control perovskite film acquired at 1.294° incidence angle. The diffraction spots belong to the residue PbI_2 which formed a trigonal structure (P-3m1 space-group) with lattice constants a = b = 4.5550 Å and c = 6.9770 Å. The crystal data are taken from the Crystallography Open Database (ID: 9009114). The three-dimensional structure indexing has been performed using GIXSGUI toolbox.[60]

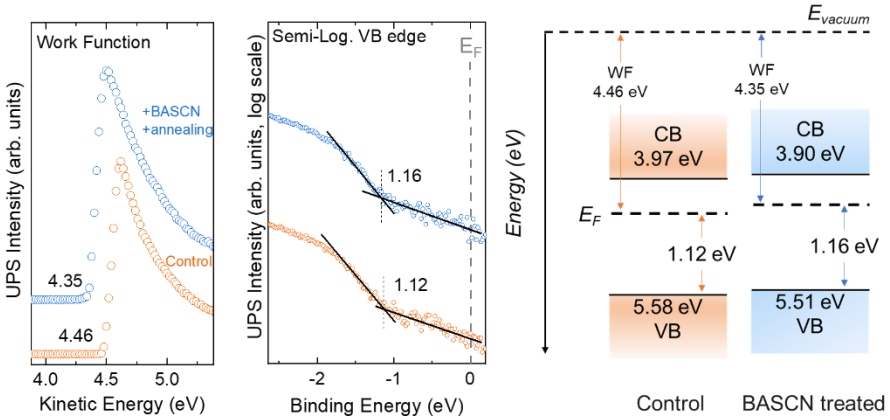

Figure S3. UPS study of the corresponding perovskite films and the schematic band diagrams of the energy levels. The perovskite is $Cs_{0.1}FA_{0.9}Pb(I_{0.9}Br_{0.1})_3$ with 2.75 mol% $PbCl_2$ as additive.

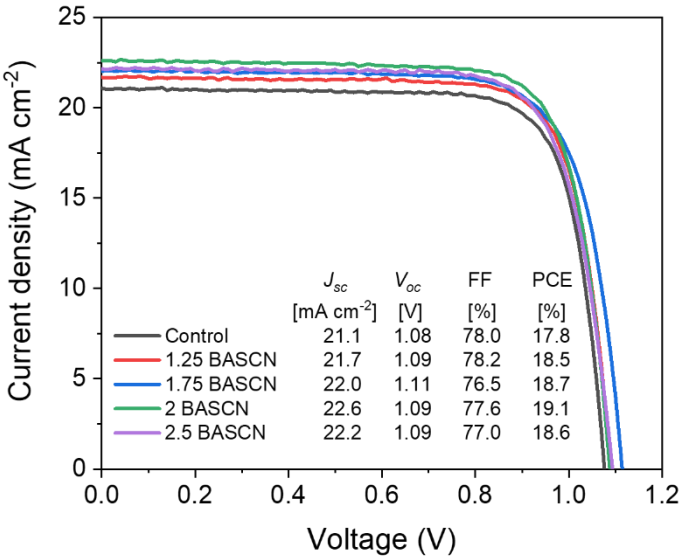

Figure S4. Reverse scan *J-V* curves of the PSCs modified by different concentrations (1.25, 1.75, 2, 2.5 mg/mL) of BASCN. The perovskite is $Cs_{0.1}FA_{0.9}Pb(I_{0.9}Br_{0.1})_3$ with 2.75 mol% $PbCl_2$ additive.

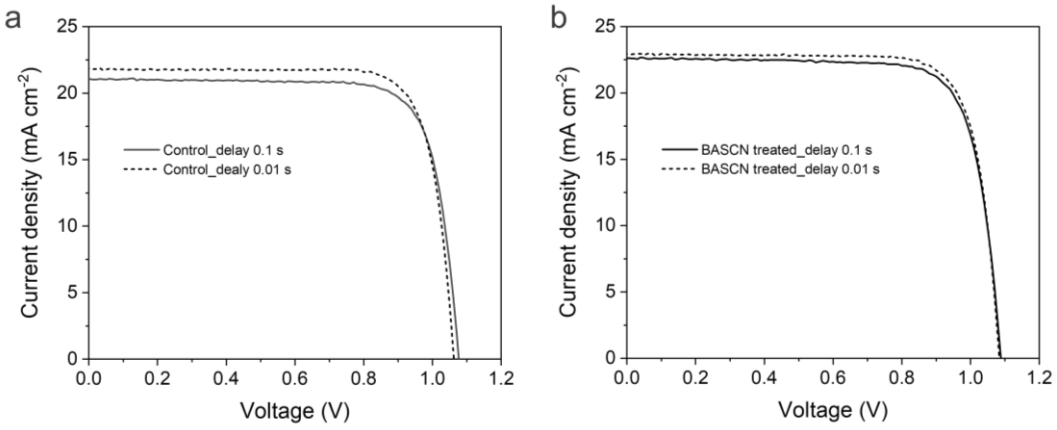

Figure S5. Reverse scan *J-V* curves of the best (a) control PSC and (b) BASCN treated PSC with measurement delay time of 0.01 s and 0.1 s, respectively. The perovskite is $Cs_{0.1}FA_{0.9}Pb(I_{0.9}Br_{0.1})_3$ with 2.75 mol% $PbCl_2$ as additive.

Table S3. Photovoltaic parameters of the control and BASCN treated PSCs.

	J_{sc} [mA cm^{-2}]	V_{oc} [V]	FF [%]	PCE [%]
Control_reverse	21.1	1.08	78.0	17.77
Control_forward	21.0	1.06	77.2	17.18
BASCN treated _reverse	22.6	1.09	77.6	19.12
BASCN treated_forward	22.4	1.08	77.2	18.68

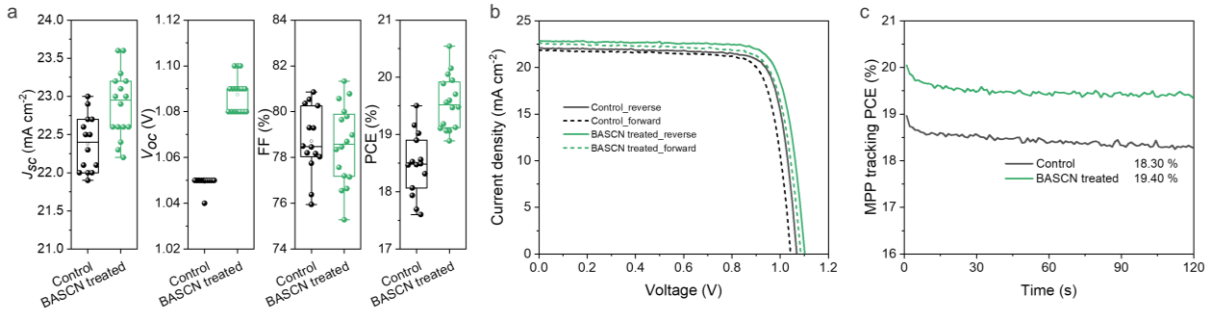

Figure S6. Device performance of the control and the BASCN treated PSCs based on $Cs_{0.1}FA_{0.9}Pb(I_{0.955}Br_{0.045})_3$ with 2.75 mol% $PbCl_2$ as additive. (a) Statistical results of J_{sc}, V_{oc}, FF and PCE, the measurement delay time is 0.01 s. The concentration of BASCN is 2.0 mg/mL. (b) Forward and reverse *J-V* curves and (c) MPP tracking performance of the corresponding PSCs.

Table S4. Photovoltaic parameters of the control and the BASCN treated PSCs.

	J_{sc} [mA cm^{-2}]	V_{oc} [V]	FF [%]	PCE [%]
Control_reverse	22.1	1.07	80.2	18.96
Control_forward	21.8	1.04	79.5	18.02
BASCN treated_reverse	22.8	1.10	80.0	20.06
BASCN treated_forward	22.6	1.09	78.1	19.24

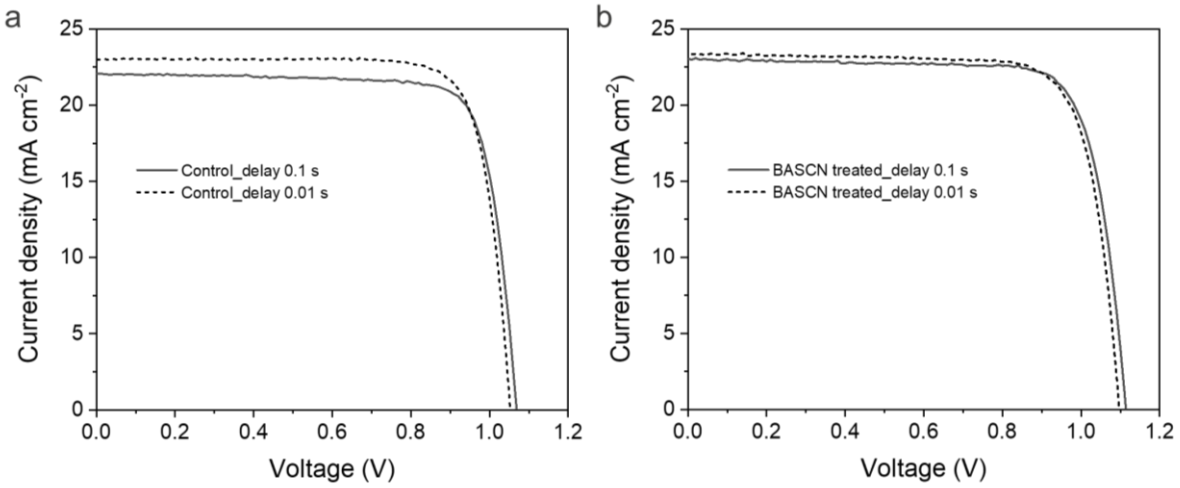

Figure S7. Reverse scan *J-V* curves of (a) the control PSC and (b) the BASCN treated PSC with measurement delay time of 0.01 s and 0.1 s, respectively. The perovskite is $Cs_{0.1}FA_{0.9}PbI_{2.865}Br_{0.135}$ with 2.75 mol% $PbCl_2$ as additive. The concentration of BASCN is 2.0 mg/mL.

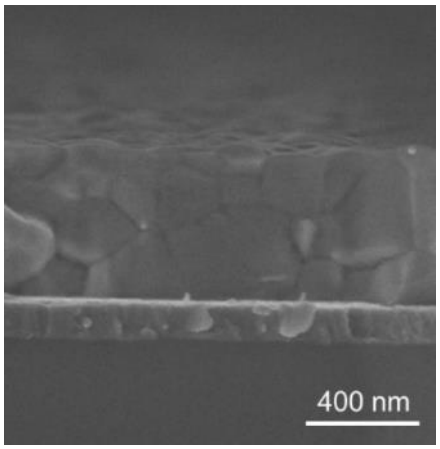

Figure S8. Cross-sectional SEM image of the control perovskite film with a set composition of $Cs_{0.1}FA_{0.9}PbI_{2.865}Br_{0.135}$ with 2.75 mol% $PbCl_2$ as additive.

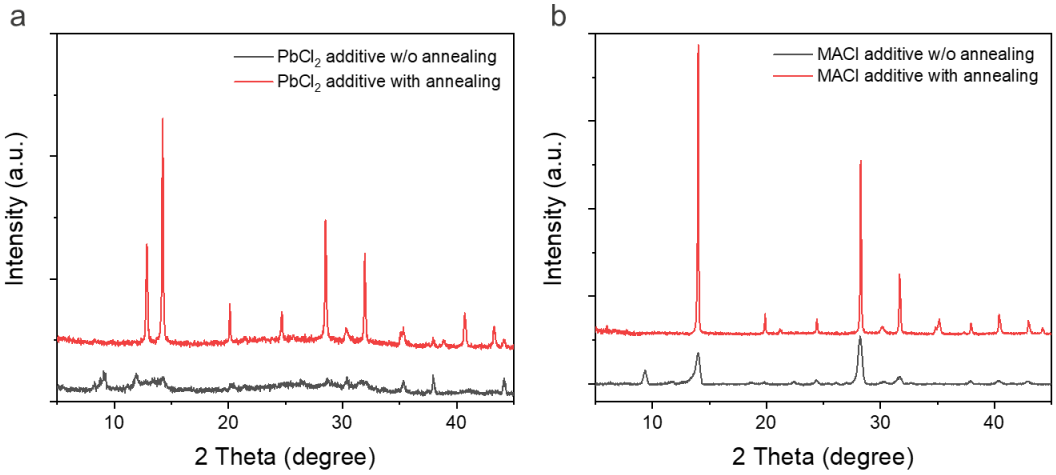

Figure S9, (a) XRD patterns of the $PbCl_2$ doped perovskite films with and without annealing. (b) XRD patterns of the MACl doped perovskite films with and without annealing.

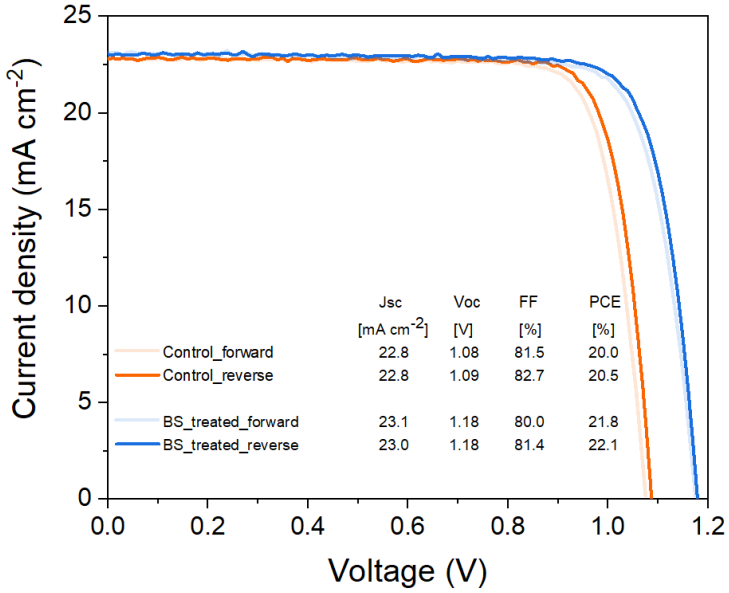

Figure S10. Hysteresis study of the champion PSCs with the measurement delay time of 0.1s. The perovskite is $Cs_{0.1}FA_{0.9}Pb(I_{0.9}Br_{0.1})_3$ with 30 mol% MACl as additive.

Table S5. Average photovoltaic parameters of the control and the BASCN treated PSCs.

	J_{sc} [mA cm^{-2}]	V_{oc} [V]	FF [%]	PCE [%]
Control	22.50	1.082	78.5	19.10
Deviation	*0.33*	*0.010*	*2.8*	*0.72*
BASCN treated	22.53	1.149	80.8	20.91
Deviation	*0.44*	*0.013*	*1.7*	*0.57*

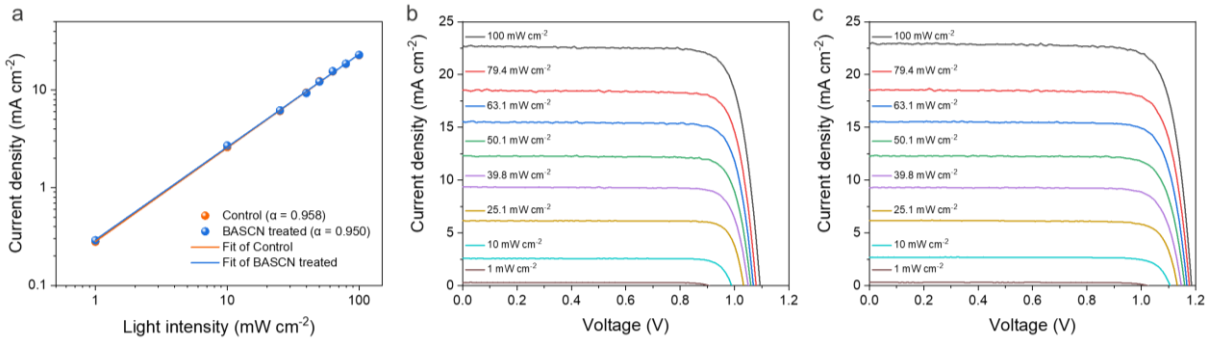

Figure S11. *J-V* responses of the control and the BASCN treated PSCs under different light intensities. (a) The relationship between the J_{sc} and light intensity for the corresponding PSCs. (b) *J-V* curves of the control PSC. (c) *J-V* curves of the BASCN treated PSC.

Table S6. Detailed *J–V* parameters of the control and the BASCN treated PSCs under different light intensity, including 100, 79.4, 63.1, 50.1, 39.8, 25.1, 10 and 1 mW cm^{-2}, defined by the optical filters.

Control	J_{sc} (mA cm^{-2})	V_{oc} (V)	FF (%)	PCE (%)
100 mW cm^{-2}	22.7	1.093	81.1	20.12
79.4 mW cm^{-2}	18.5	1.079	82.4	
63.1 mW cm^{-2}	15.5	1.069	82.4	
50.1 mW cm^{-2}	12.3	1.060	83.0	
39.8 mW cm^{-2}	9.4	1.049	83.6	
25.1 mW cm^{-2}	6.1	1.032	86.1	
10 mW cm^{-2}	2.6	0.989	85.1	
1 mW cm^{-2}	0.28	0.901	86.4	
BASCN treated	J_{sc} (mA cm^{-2})	V_{oc} (V)	FF (%)	PCE (%)
100 mW cm^{-2}	22.9	1.184	82.1	22.26
79.4 mW cm^{-2}	18.6	1.176	82.0	
63.1 mW cm^{-2}	15.6	1.167	82.2	
50.1 mW cm^{-2}	12.2	1.159	82.9	
39.8 mW cm^{-2}	9.3	1.147	83.3	
25.1 mW cm^{-2}	6.2	1.132	83.6	
10 mW cm^{-2}	2.7	1.106	83.4	
1 mW cm^{-2}	0.29	1.022	84.5	

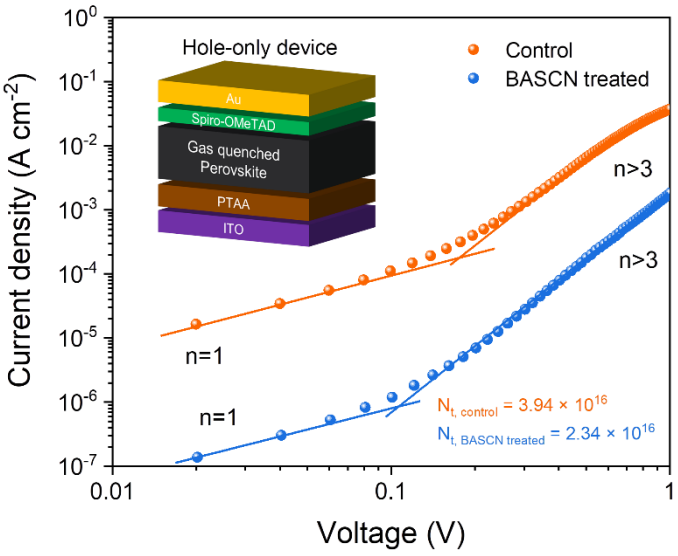

Figure S12. Dark *J-V* curves of the hole-only devices based on the control and the BASCN treated perovskite films. The inset shows the device structure of ITO/PTAA/perovskite/spiro-OMeTAD/Au.

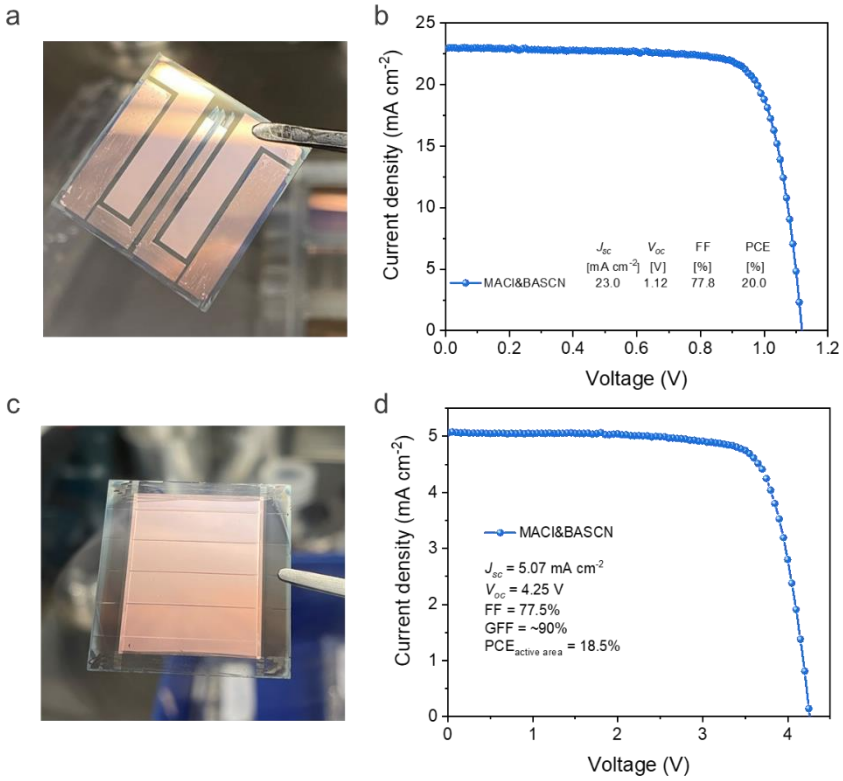

Figure S13. Larger scale device applications. (a) The photograph of the 1 cm^2 PSC. (b) Reverse scan *J-V* curve of the 1 cm^2 PSC. (c) The photograph of the 4 cm^2 perovskite mini-module with a geometric fill factor of ~90%. (d) Reverse scan *J-V* curve of the 4 cm^2 perovskite mini-module.

References:

[1] L. Rakocevic, F. Ernst, N. T. Yimga, S. Vashishtha, T. Aernouts, T. Heumueller, C. J. Brabec, R. Gehlhaar, J. Poortmans, *Sol. RRL* **2019**, *3*, 1970024.

[2] K. Elkhouly, I. Goldberg, H.-G. Boyen, A. Franquet, V. Spampinato, T.-H. Ke, R. Gehlhaar, J. Genoe, J. Hofkens, P. Heremans, W. Qiu, *Adv. Opt. Mater.* **2021**, 2100586.

[3] H. Amenitsch, M. Rappolt, M. Kriechbaum, H. Mio, P. Laggner, S. Bernstorff, *J. Synchrotron Radiat.* **1998**, *5*, 506.

[4] M. Burian, C. Meisenbichler, D. Naumenko, H. Amenitsch, *arXiv:2007.02022*.

[5] Z. Jiang, *J. Appl. Crystallogr.* **2015**, *48*, 917.

[6] J. H. Scofield, *J. Electron Spectros. Relat. Phenomena* **1976**, *8*, 129.

[7] A. Proctor, P. M. A. Sherwood, *Anal. Chem.* **1982**, *54*, 13.